




Pushing the boundaries
of chemistry?
It takes
#HumanChemistry

Make your curiosity and talent as a chemist matter to the world with a specialty chemicals leader. Together, we combine cutting-edge science with engineering expertise to create solutions that answer real-world problems. Find out how our approach to technology creates more opportunities for growth, and see what chemistry can do for you at:

[evonik.com/career](https://www.evonik.com/career)



Macro-porous permeability aspects of MgSO₄ salt hydrate foams for energy storage applications

Luigi Calabrese¹  | Leonor Hernández² | Rosa Mondragón² | Luisa F. Cabeza³

¹Department of Engineering, University of Messina, Messina, Italy

²Departamento de Ingeniería Mecánica y Construcción, Universitat Jaume I, Campus de Riu Sec, Castellón de la Plana, Spain

³GREiA Research Group, Universitat de Lleida, Lleida, Spain

Correspondence

Luigi Calabrese, Department of Engineering, University of Messina, Contrada di Dio Sant'Agata, Messina 98166, Italy.
Email: lcalabrese@unime.it

Funding information

ICREA; Ministerio de Ciencia, Innovación y Universidades - Agencia Estatal de Investigación, Grant/Award Number: RED2018-102431-T; Ministerio de Ciencia, Innovación y Universidades de España (MCIU/AEI/FEDER, UE), Grant/Award Number: RTI2018-093849-B-C31

Abstract

In the present work a macroporous silicone foam, able to contain the magnesium sulfate, was chosen as matrix for the reversible hydration/dehydration process of the salt hydrate. The aim of the article was addressed towards the assessment of the relationship among microstructure, permeability and mass diffusion of the composite foam. This aspect represents an essential step for the future industrial development of this composite material. The results show that the filler content influences the foam morphology where a transition from closed to mixed and then closed cell again was observed with increasing filler content. Consequently, depending on the distribution and interconnection of the structural channels, a different effectiveness in guaranteeing mass diffusion phenomena was identified. In particular, permeability tests show that foams with 50 wt% of salt hydrates have a highly interconnected microstructure allowing a permeability over three times higher than a closed cell structure making it suitable for thermochemical energy storage applications.

KEYWORDS

composite foams, foam morphology, permeability, salt hydrate, thermochemical energy storage

1 | INTRODUCTION

Thermal energy storage (TES) technologies are a valid counterpart to various renewable energy sources (RES) and are also able to valorize waste heat in order to reduce the building energy demand.¹ The energy can be stored by several different technologies such as sensible heat, latent heat or even as physical or chemical energy (i.e., thermo-chemical energy storage).² In this latter, reversible chemical and physical reactions are exploited to recover the heat exchanged during the reaction.

Salt hydrates are a promising class of materials, based on hydration/dehydration reactions, to apply this technology at low-to-medium temperature operating range (i.e., 70–150°C).³ Salt hydrates are a most attractive solution

to store low-grade heat due to their high-energy storage density, theoretically indefinitely long-term storage capability, separation of reactants using water vapor as a safe and cheap gaseous sorbate.⁴ This implied that this class of materials has been extensively investigated⁵ allowing to define a database of materials and their chemical-physical and storage density properties^{5,6} as well as to evaluate the application in laboratory-scale reactors.⁴

However, several problems arise when these materials are used in a storage system limiting their field of applicability. The coupled agglomeration and swelling phenomena, occurring during de/hydration cycles, imply a reduction in vapor diffusion and favor the material degradation⁷ representing a critical point to consider. Furthermore, the high corrosiveness of these materials is a

This is an open access article under the terms of the Creative Commons Attribution-NonCommercial License, which permits use, distribution and reproduction in any medium, provided the original work is properly cited and is not used for commercial purposes.

© 2021 The Authors. *Journal of Applied Polymer Science* published by Wiley Periodicals LLC.

thoughtful drawback in the use of salt hydrates in a thermal storage plant. To overcome these issues, a potentially effective approach, proposed in the literature, is the dispersion of salt in a host matrix.

Concerning the active filler in the composite matrix, magnesium sulfate heptahydrate ($\text{MgSO}_4 \cdot 7\text{H}_2\text{O}$) has been identified as a suitable candidate for TES due to its storage temperature, high energy density, availability, low cost, and non-toxicity.^{8,9} Among the different options as hosting matrix, adsorbent porous materials (zeolite, mesoporous silica, porous carbon compounds) have often been proposed as appropriate choice.^{10–12}

Hongois et al.¹³ investigated zeolite– MgSO_4 composites relating chemo-physical and de/hydration properties. The results evidenced that the active material was dispersed in the matrix optimizing the gas–solid reaction kinetics and the thermal power released/absorbed. Furthermore, the composite exhibited an energy density of 150–400 kWh/m³ in a temperature range compatible with solar-thermal collectors. In Porosen et al.,¹⁴ magnesium sulfate was embedded in various porous host materials (pore diameters from 1.7 μm to 7 nm) showing an effective hydration of the MgSO_4 salt was acquired evidencing furthermore an increase of the heat of adsorption increasing the pore size.

Analogously, Xu et al.¹⁵ evaluated the hydration behavior of MgSO_4 filled in 13X zeolite for long term heat storage. The results showed that the composite had larger hydration ability than pure zeolite, and the reactor filled with the 13X zeolite- MgSO_4 composites evidenced a good cyclability and an energy efficiency equal to 81.34%.

Xu et al.¹⁶ developed composite sorbents of MgSO_4 filled in zeolite 13X and activated alumina TES applications. The results evidenced that the impregnated MgSO_4 salt hydrate improves the TES performances of both 13X zeolite and activated alumina, significantly improving the temperature-rising rate of the zeolite and the temperature lift of activated alumina.

A similar approach was assessed by Wang et al.¹⁷ indicating a composite material with MgSO_4 a promising option for long-term thermochemical heat storage.

Similarly interesting results were found by evaluating expanded graphite as host container of the salt hydrates.^{12,18} Recently, Ousaleh et al.¹⁹ proposed a new thermochemical material using silica gel as a host material and impregnated with different salt hydrates (30 wt% of MgSO_4 , CuSO_4 , and $\text{Al}_2[\text{SO}_4]_3$) evidencing a storage density in the range of about 600–800 kJ/kg.

In this concern, the use of matrix foams with large pore size and volume is becoming a promising approach to encapsulate salt hydrates for thermochemical energy storage in order to prevent agglomeration and to enhance

the material stability.^{20,21} Korhammer et al.²² evaluated the impregnation of CaCl_2/KCl into activated carbon foam and expanded natural graphite leading to an improvement both of the thermal conductivity and the dehydration/hydration behavior. Analogously, Wu et al.²³ investigated a porous hydroxyapatite foams as carrier of hydrated salt for thermal energy storage. The results showed that the composite material had well chemical stability and thermal stability.

In summary, composites allow a performance improvement of the pure salts, in terms both of thermo-physical and kinetic properties, also allowing to improve the material stability and durability for a high-efficient use for low-grade thermal energy systems.²⁴

However, the usually used matrices have a rigid and brittle structure. This could lead to long-term stability issues, due to the triggering of internal stresses in the host matrix due to the expansion of the saline solution during the hydration step that limit the material stability.^{25,26} Furthermore, the matrices have usually an open porosity, which (especially for composites with large amount of salt) is not able to retain the hydrated solution in case of supersaturation, causing a release of the salt with consequent loss of efficiency as well as degradation and corrosion risks for the reactor.¹⁹

Instead, polymeric foams, characterized by a flexible and ductile structure, are able to suffer the volume expansion induced by the salt hydration. Furthermore, some polymeric foams are characterized by a good water vapor permeability that allows hydration/dehydration phases also for active fillers confined inside a closed porosity.^{27,28}

For instance, recently, Brancato et al.²⁹ proposed an innovative concept of composite for energy storage applications. In particular, a macroporous silicone foamed structure was used as host matrix of the salt hydrate. The silicone foam facilitates of water vapor diffusion and prevents agglomeration of the active filler during hydration.³⁰ Furthermore, in Ref. 31 the good mechanical stability and the limited salt hydrate loss after 50 de/hydration cycles was addressed.

The aim of present article is to further develop this concept, by assessing the permeability properties and morphological microstructure of the $\text{MgSO}_4 \cdot 7\text{H}_2\text{O}$ – silicone composite foams. The analysis of mass transport phenomena and their correlation with the microstructure of the material is highly required to evaluate its applicability in a real scale context. Foamed composites with different amount of $\text{MgSO}_4 \cdot 7\text{H}_2\text{O}$ (40–70 wt%) were synthesized. Foam microstructure was evaluated by 3D optical and electron scanning microscopy and digital image analysis. Permeability measurements at varying flow rate were performed to assess the mass flow capability of the composite foams.

2 | EXPERIMENTAL PART

2.1 | Foam preparation

Macro porous composite materials were obtained applying a direct foaming approach of a siloxane-based matrix, according to the procedure reported in Ref. 32. The siloxane matrix was chosen for its high water vapor permeability that, considering also a porous foamed morphology, should favor the diffusion of water vapor during real operating conditions.³³

The siloxane matrix is composed by a hydroxyl terminated polydimethylsiloxane (PDMS, M_w 110,000 CAS: 70131-37) coupled to a poly(methylhydrosiloxane), PMHS, M_w 1400-1800 CAS: 63148-57-2 that acts as crosslinker and foaming agent. Both compounds were supplied by Gelest Inc. (Morrisville). In particular, the composite foam preparation was carried out in five steps: (a) preliminarily, the $MgSO_4 \cdot 7H_2O$ salt hydrate (Merck, Germany, density 1.68 g/cm^3) was dispersed under magnetic stirring in polydimethylsiloxane (PDMS) compound for about 60s; (b) in order to increase slurry workability two different solvents were added: water (50 wt%) and ethanol (25 wt%); (c) afterwards, the poly-methylhydrosiloxane compound (PMHS, 2:1 PMHS:PDMS mass ratio) was added to the mixture always under magnetic stirring for about 60 s; (d) as final mixing step, tin(II) 2-ethylhexanoate (Sn(II)) (d:1.12, M_w 405.11, 50%, CAS. 301-10-0) as catalyst was added under vigorous mixing, for about 15 s; and (e) finally, the so obtained slurry was carefully poured into a cylindrical closed mold and cured at 60°C for 24 h to complete the foaming process. The foaming process was obtained by dehydrogenative coupling reaction between

PDMS and PMHS siloxane compounds. Details concerning the foaming mechanisms of siloxane matrix can be found in Ref. 34. A scheme of the synthesis steps of the salt hydrate composite foams is shown in Figure 1.

In this experimental set-up a shape-controlled sample by using a closed mold was carried out. Despite the open mold technology, applied in our previous experimental approaches,²⁹⁻³² it was required to have a suitable control of the sample geometry. Although this choice could influence the foam morphology at varying filler content, requiring a new microstructural analysis to well define the pore size and distribution of the samples.

Salt hydrate filler at varying content (40–70 wt% of PDMS+PMHS compounds) were realized. Detail of all the synthesis compounds ratio is reported in Table 1. As blank, an unfilled silicone foam was prepared. All samples were coded by using a “MgF-” acronym coupled to a number indicating the salt hydrate content (in percentage) as obtained in the composite foam. For instance, the MgF-40 batch is referred to composite samples made with 40% of $MgSO_4 \cdot 7H_2O$ salt hydrate. The code MgF-0 indicates the unfilled polymeric foam. On the slurry solution viscosity measurements were carried out by using a digital rotational viscometer (NDJ-5S Vevor, Italy) performing measurements for 1 min at 30 rpm at room temperature and in open to air conditions.

2.2 | Foam morphology and microstructure

Foam morphology and surface characteristics were evaluated preliminarily by optical 3D digital microscopy

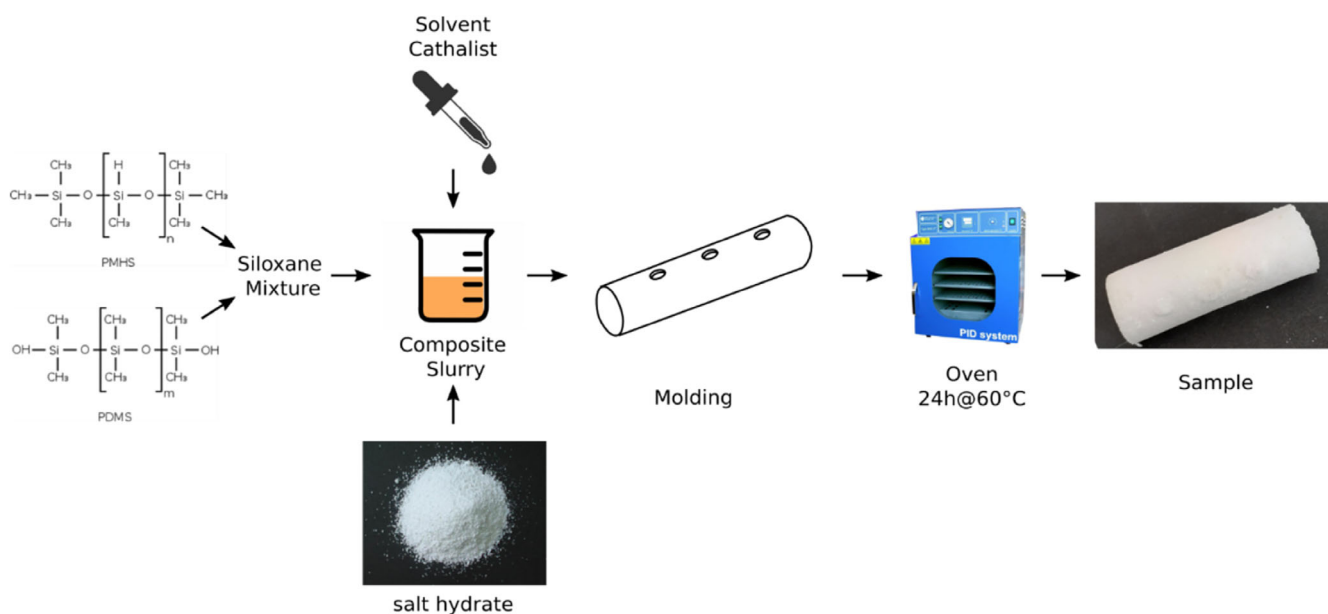


FIGURE 1 Scheme of the synthesis steps of the salt hydrate composite foams [Color figure can be viewed at wileyonlinelibrary.com]

		MgF-0	MgF-40	MgF-50	MgF-60	MgF-70
PDMS	Siloxane	24.4%	16.4%	14.1%	11.6%	9.0%
PMHS	Siloxane	48.8%	32.8%	28.2%	23.2%	18.0%
Water	Solvent	12.2%	8.4%	7.0%	5.8%	4.5%
Ethanol	Solvent	6.1%	4.0%	3.5%	3.0%	2.3%
Sn(II)	Catalyst	8.5%	5.6%	4.9%	4.1%	3.2%
MgSO ₄ ·7H ₂ O	Filler	0.0%	32.8%	42.3%	52.3%	63.0%
Salt hydrate/foam (wt%)		0.0%	40.0%	50.0%	60.0%	70.0%

TABLE 1 Siloxane solution compositions at varying salt hydrate content (percent by weight)

(Hirox HK-8700) in order to macroscopically evaluate the foam homogeneity and structural regularity. Furthermore, field emission scanning electron microscopy (SEM) (JEOL 7001F) was performed to better assess the composite foam cellular structure and the local hydrate salt polymer matrix interaction.

2.3 | Bubble size distribution

In order to correlate the permeability capacities with the foam microstructure, a quantitative study of the shape and distribution of the bubbles in the microporous foams was carried out by means of digital image analysis performed on SEM images on sample cross sections (optical 3D digital microscope - Hirox HK-8700). For each batch two contiguous images were chosen to improve the analysis area and minimize the amount of partially viewed bubbles.³⁵ The analysis was performed on a total view spanning of about 8 mm × 6 mm.

Due to an inhomogeneous contrast of the bubble contour, it was not possible to apply automatic particle discrimination protocols. Instead, the digital image processing was performed by a semi-automatic procedure: at first, the outline of each bubble was identified and marked manually using a photo editing program (Gimp 2.8), finally an image analysis software (ImageJ 1.48, WS Rasband, ImageJ, US National Institutes of Health) was used to estimate the numerosity and relative geometric characteristics of all bubbles. The bubble data distribution was clustered in classes calculating their number, N_C , and interval, w_C , according to the Sturges rule³⁶:

$$N_C = \log_2(N_b) + 1 \quad (1)$$

$$w_C = \frac{d_{\max} - d_{\min}}{N_C} \quad (2)$$

where N_b is the number of bubbles, d_{\max} and d_{\min} are the measured equivalent diameters of the largest and smallest measured bubbles, respectively.

2.4 | Permeability tests

Permeability tests on the composite foams were carried out by means of an experimental set-up design to do the analysis. As shown in Figure 2, the set-up consists of a test section made of Teflon, PTFE, (2 cm height and 2.5 cm of diameter) where the sample is introduced. This section is assembled in between two stainless steel sections with constant diameter of 2.5 cm to allow the air flow. A pressure sensor is installed in the lower part, before the test section, while the upper part is open and atmospheric pressure is established. Different pressure sensors were used depending on the experimental pressure drop: up to 1.5 kPa (Gems Sensors, Inc.) and up to 0.4 bar (model cb2021, LABOM Mess- und Regeltechnik GmbH). The air passes through a drierite desiccant cartridge to ensure dry conditions and then enters the set-up through the bottom part. A flow meter with a maximum flow rate of 10 L/min (Bronkhorst High-Tech B.V) is used to control the air flow rate. Pressure drop, air temperature and air flow rate were registered by means of an acquisition system.

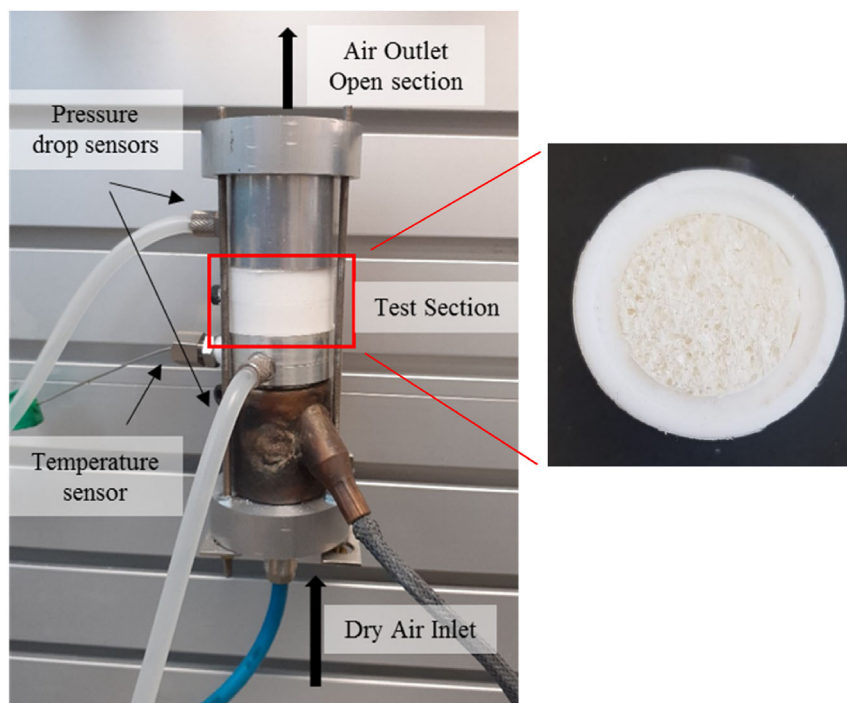
Before the tests, the samples were dried 24 h in the oven at 130°C and then kept in a desiccator to remove moisture content and to ensure initial constant conditions of humidity and temperature. The tests were carried out at different flow rates from 1 to 10 L/min.

3 | RESULTS AND DISCUSSION

3.1 | Morphological analysis

Preliminarily, the homogeneity and regularity of the foam was evaluated in order to assess structural uniformity and macro-defect free morphology. A compact and uniform foam structure, coupled with an intrinsic interconnected porosity, represent a fundamental condition for identifying a potential application efficacy of these materials in this application context. In this regard, a parametric morphological evaluation of the foam (e.g., size, shape,

FIGURE 2 Experimental set-up for permeability tests and top view of the test section [Color figure can be viewed at wileyonlinelibrary.com]



and distribution of the bubbles) are relevant aspects that must be taken into consideration.

Figure 3 shows optical images of a reference cross section of foamed samples at increasing $\text{MgSO}_4 \cdot 7\text{H}_2\text{O}$ filler content. The white arrow indicates the foaming direction.

Visually evaluating the bubble distribution, an almost regular morphology can be addressed. The foaming is a dynamic and in a continuous evolution process with a progressive formation and growth of hydrogen bubbles (product of the reaction between the siloxane compounds – PDMS and PMHS) which progressively evolves upwards in the composite slurry. The growth of the bubble is due to a dual contribute: (a) the increase in internal pressure that takes place following the siloxanes reaction and (b) the coalescence phenomena that take place as a consequence of the physical aggregation of the bubble during their motion.³⁰ Although there are many factors competing in the growth and orientation of the bubbles, evaluating the sample cross sections along the foaming direction, from a basic visual point of view, no preferential location or shape orientation on bubbles can be observed. This indicates a homogenous and regular foaming stage that uniformly occurred on the whole mold areas.

Composite foams with high filler content (MgF-60; MgF-70) are quite dense and compact. Indeed, composite foams with low filler content (MgF-40; MgF-50) appears with larger bubbles homogeneously distributed on the whole cross-section. Some large cavities were also identifiable (Figure 3b and Figure 3c).

Although, it is worth noting some local heterogeneities for MgF-40 sample (Figure 3b). In particular, there are some relatively large and irregularly shaped bubbles in the lower area of the specimen. A clear heterogeneity in the distribution of the filler is also evident. This behavior is attributable to the different foaming process that occurs for composite slurry at different salt hydrate content.

In this batch some bubbles on the bottom side are slightly larger and elliptically depressed than the top side. At the same time, a salt hydrate sedimentation takes place. This behavior could be attributable to the lower salt content in this formulation, which implies a reduced viscosity of the composite slurry. Consequently, during the foaming process there is a significant flow of bubbles that originate, coalesce and evolve towards the surface. This, associated with the low viscosity of the slurry in the early stages of solidification, implies a gradual depletion in salt hydrate content on the top side of the mold and subsequent salt precipitation towards the bottom of the mold (favored by the low settling time of the filler in the low viscosity slurry). The filler precipitation stimulates the bubbles elongation and depression, as visually observed in Figure 3b. These considerations are confirmed in Table 2 where the viscosity evolution of the composite siloxane solution at increasing salt content is reported.

Further consideration can be acquired evaluating, at higher magnification, the foam microstructure morphology and interfacial filler matrix interaction.

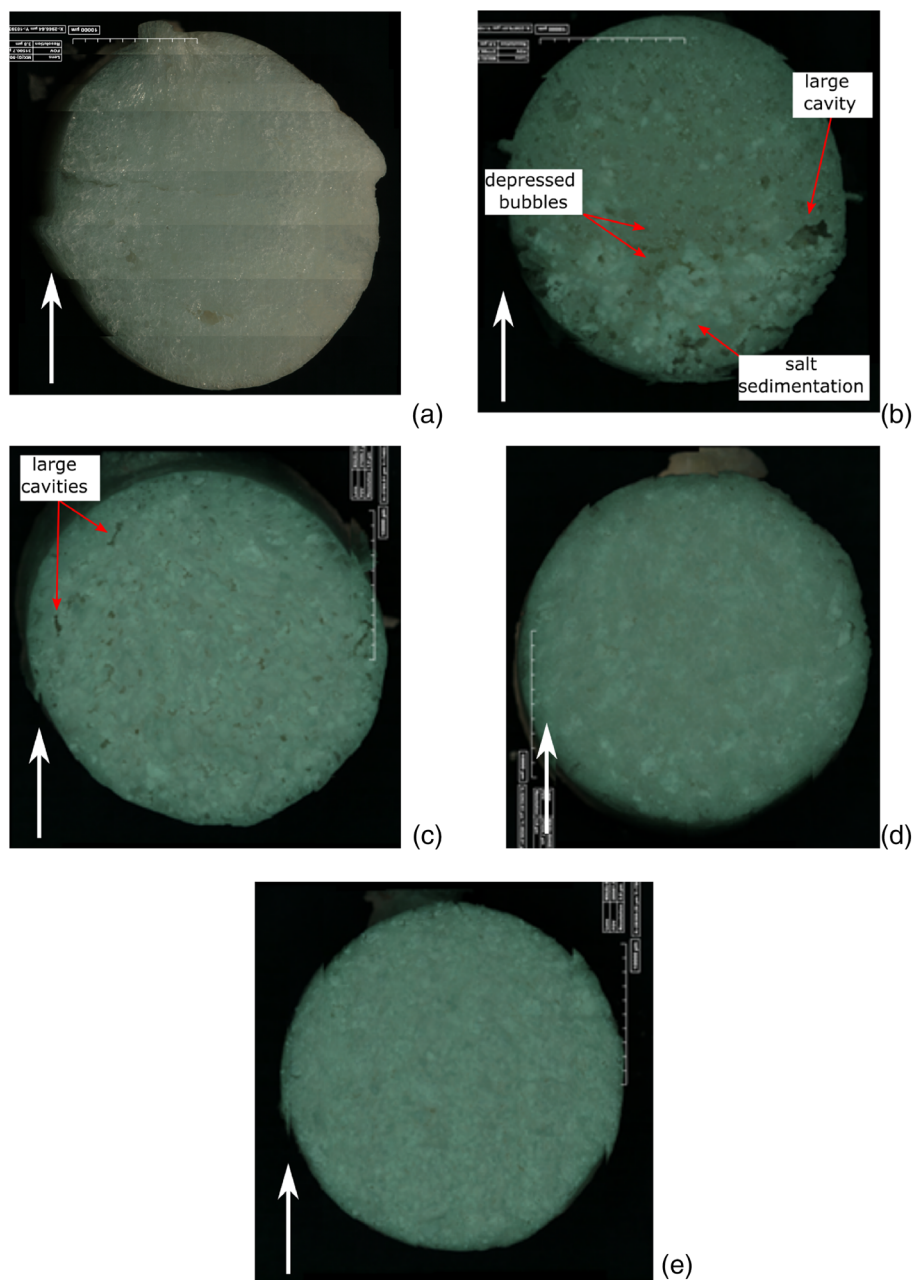


FIGURE 3 Stereo-microscopy image of cross-section of siloxane foams at varying salt hydrate content: (a) MgF-0; (b) MgF-40; (c) MgF-50; (d) MgF-60; (e) MgF-70 [Color figure can be viewed at wileyonlinelibrary.com]

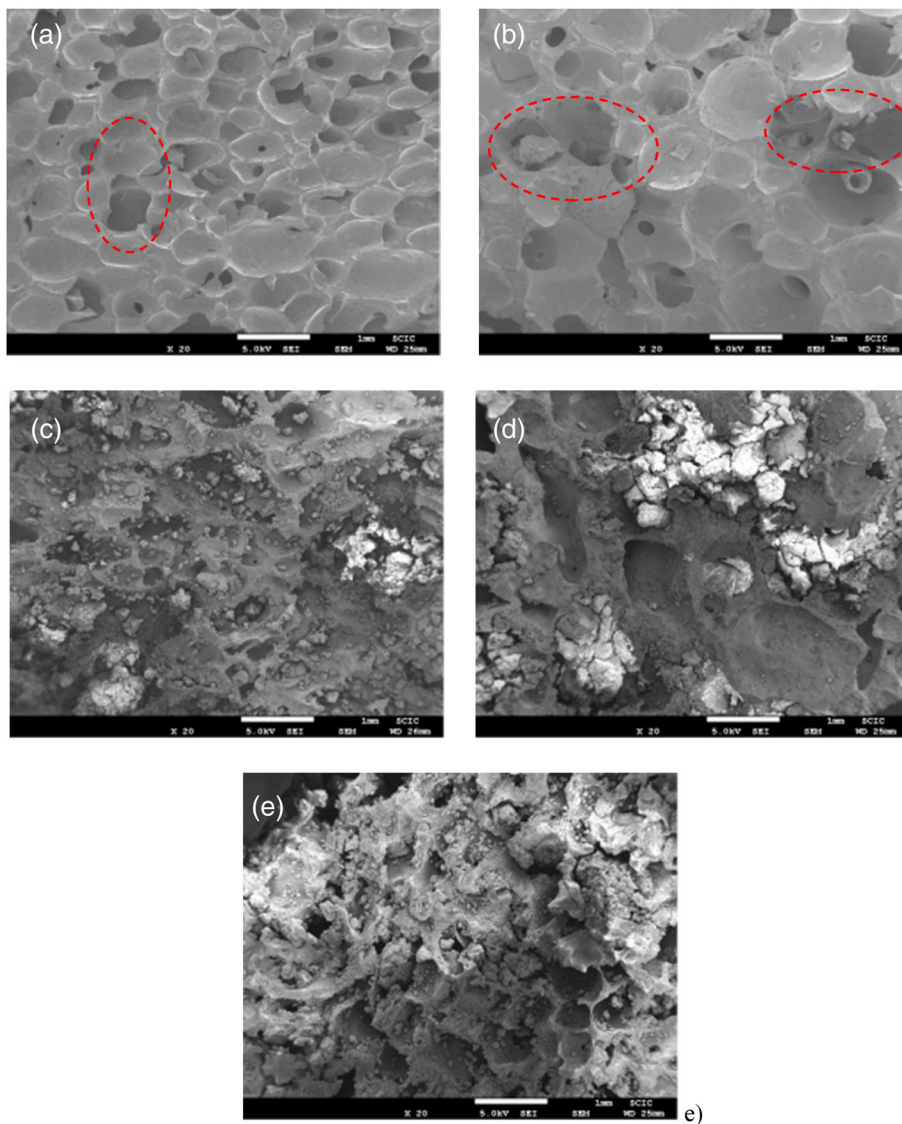
	MgF-0	MgF-40	MgF-50	MgF-60	MgF-70
Salt hydrate/foam (wt%)	0.0%	40.0%	50.0%	60.0%	70.0%
Viscosity (mPa s)	189	982	1744	3984	7785

TABLE 2 Viscosity of composite siloxane solution at varying salt hydrate content

Figure 4 shows SEM images of siloxane foams at increasing salt hydrate content. Unfilled siloxane foam, MgF-0 (Figure 4a) has a regular structure with well-defined bubbles. A mainly closed cell structure can be identified. In fact, only some bubbles are locally interconnected each other, as identifiable in circled area in Figure 4a. The addition of salt hydrates leads to a

progressive modification of the cellular microstructure of the foam. The MgF-40 foam (Figure 4b), characterized by the lowest amount of $\text{MgSO}_4 \cdot 7\text{H}_2\text{O}$, shows a morphology apparently compatible with that found for unfilled foam. However, it should be noted that the bubbles in MgF-40 sample have larger dimensional heterogeneity than MgF-0 one. A large distribution of

FIGURE 4 Scanning electron microscopy images of siloxane foams at increasing salt hydrate content: (a) MgF-0; (b) MgF-40; (c) MgF-50; (d) MgF-60; (e) MgF-70 [Color figure can be viewed at wileyonlinelibrary.com]



bubble size is detectable. The observed morphology evidenced that the addition of the $\text{MgSO}_4 \cdot 7\text{H}_2\text{O}$ enhanced the foaming process, possibly due to the interaction of the salt hydrates with the reactive hydride and hydroxyl groups of the siloxane compounds. This reactivity leads to large bubbles growth. Furthermore, due to low viscosity of the composite slurry, coalescence phenomena occurred as a consequence of bubbles aggregation.

However, comparing the morphology with that found for unfilled foam, a greater quantity of secondary channels between the bubbles is clearly evident, warranting a very widespread continuous interconnected bubble network. These channels trigger preferential tortuous pathways among the bubbles for the water vapor diffusion during the salt hydration/dehydration phase. This feature is potentially effective for use in sorption thermochemical energy storage technology.

At increasing $\text{MgSO}_4 \cdot 7\text{H}_2\text{O}$ filler content, the coalescence phenomenon is gradually inhibited. This aspect is evident in Figure 4e referred to MgF-70 foam. The structure composite foam with the highest salt hydrate content is characterized by small-size bubbles apparently with low interconnections. No regular preferential pathways can be identified. The high quantity of salt strongly hinders the microstructural stability of the foam. The bubbles growth is very heterogeneous and irregular. The filler interpenetrates with the intrinsic porous structure of the foam, increasing the internal tortuosity. Furthermore, local defects, detachments and cracks have been found in correspondence to bubble walls or struts, further adversely affecting the structural regularity of the foam.

Indeed, a more articulate discussion is required to interpret the morphology of MgF-50 batch (Figure 4c). The structure is complex and not homogeneous. The salt content is distributed almost uniform within the material

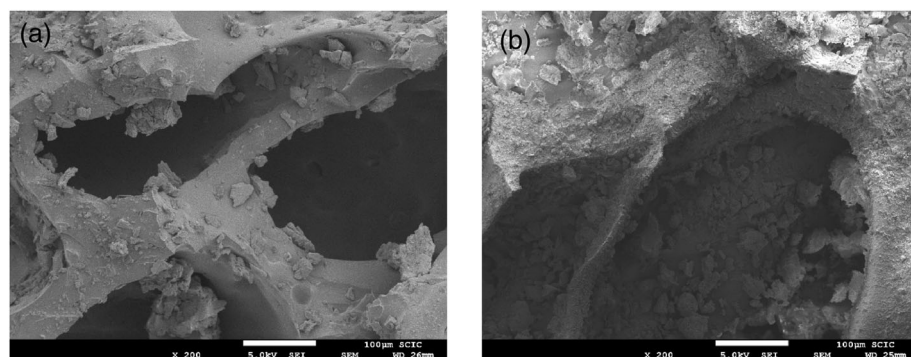


FIGURE 5 High magnification scanning electron microscopy image of siloxane foams (a) MgF-50; (b) MgF-70

bulk. Only local and limited agglomeration areas of the filler take place. Figure 5 shows high magnification SEM images for MgF-50 and MgF-70 in which the differences in the salt distribution is clearly observed. In the MgF-50 the salt remains at the walls of the cells but does not fill the inner part of the pores while in the MgF-70 sample the salt is inside the pores clogging them and thus reducing the overall porosity.

Evaluating the distribution of walls/struts and bubbles the foam assumes a co-continuous-like structure with the bubbles intercalated in the polymeric matrix. Many contiguous bubbles appear with a macro-bubble, characterized by a non-regular geometry with multiple extensions and shrinks due to the absence of discontinuity points among contiguous bubbles. This morphological structure is typical of systems that have had the activation but not the completion of the bubble coalescence. Therefore, some bubbles have a relevant dimension cause of the aggregation of multiple bubbles into larger colonies, which potentially facilitate the flow of water vapor. Furthermore, the presence of some secondary channels has a beneficial role on the hydration process and dehydration of the salt. At the same time, the suitable content of salt hydrates allows to hypothesize an effective stored energy density of the composite material.⁷

The qualitative morphological analysis of the samples, obtained in this section with the SEM images, requires a deeper study of the foam morphologies, which is then performed via a statistical analysis of these images.

3.2 | Statistical analysis of bubble size distributions

In order to better understand the effect of the salt hydrates content on the macro-porous structure of the silicone foam, a statistical analysis on the morphological characteristics of the bubbles was carried out. On the basis of the distribution of the bubbles, obtained by

digital analysis of the images, a study was performed aimed to quantitatively correlate the morphological parameters of the foam with its constituents.

In Figure 6, the circularity versus diameter distribution is reported for all composite foams (MgF-0, MgF-40, MgF-50, MgF-60, and MgF-70). As reference, an outlines distribution acquired by digital image analysis was also added (Figure 6, left).

The amount of salt hydrate clearly influences the bubble size and distribution in the composite foam. In particular, in the composite foam with intermediate filler content (MgF-50) a co-continuous morphology can be observed. The bubbles are not regular and are characterized by a tortuous perimeter, due to the partial coalescence of peripheral bubble during the foaming stage.

These considerations were summarized in Figure 7 where the evolution of cell size diameter and circularity (defined as $\frac{4\pi \cdot \text{Area}}{(\text{Perimeter})^2}$ – a value equal to 1.0 indicates a perfect circle; as much the value approaches 0.0 how much not regular is its shape) at increasing salt content is reported. The average bubble diameter increases due to salt hydrate addition in the PDMS foam. Just adding 40 wt% of filler, an increase of about 25% of bubble size was observed. At very large salt hydrate content, a new abrupt reduction on the average bubble size can be, furthermore, observed.

This result is apparently not consistent with to the previous one in Ref. 30. However, it is worth noting that in this sample preparation set-up a closed mold was used. This implies that the foaming process the composite material is confined in a well-defined space. This phenomenon is all the more evident the higher the foaming ratio (in open to air conditions) of the composite slurry. The unfilled silicone foam (MgF-0) resulted in previous experience characterized by very large foaming ratio.³⁰ Therefore, during the reaction, several bubbles triggered and growth leading to a large foamed structure. This phenomenon could not be completed for a closed mold configuration. Therefore, for MgF-0 batch, the bubble foaming process had to be blocked due to the presence of

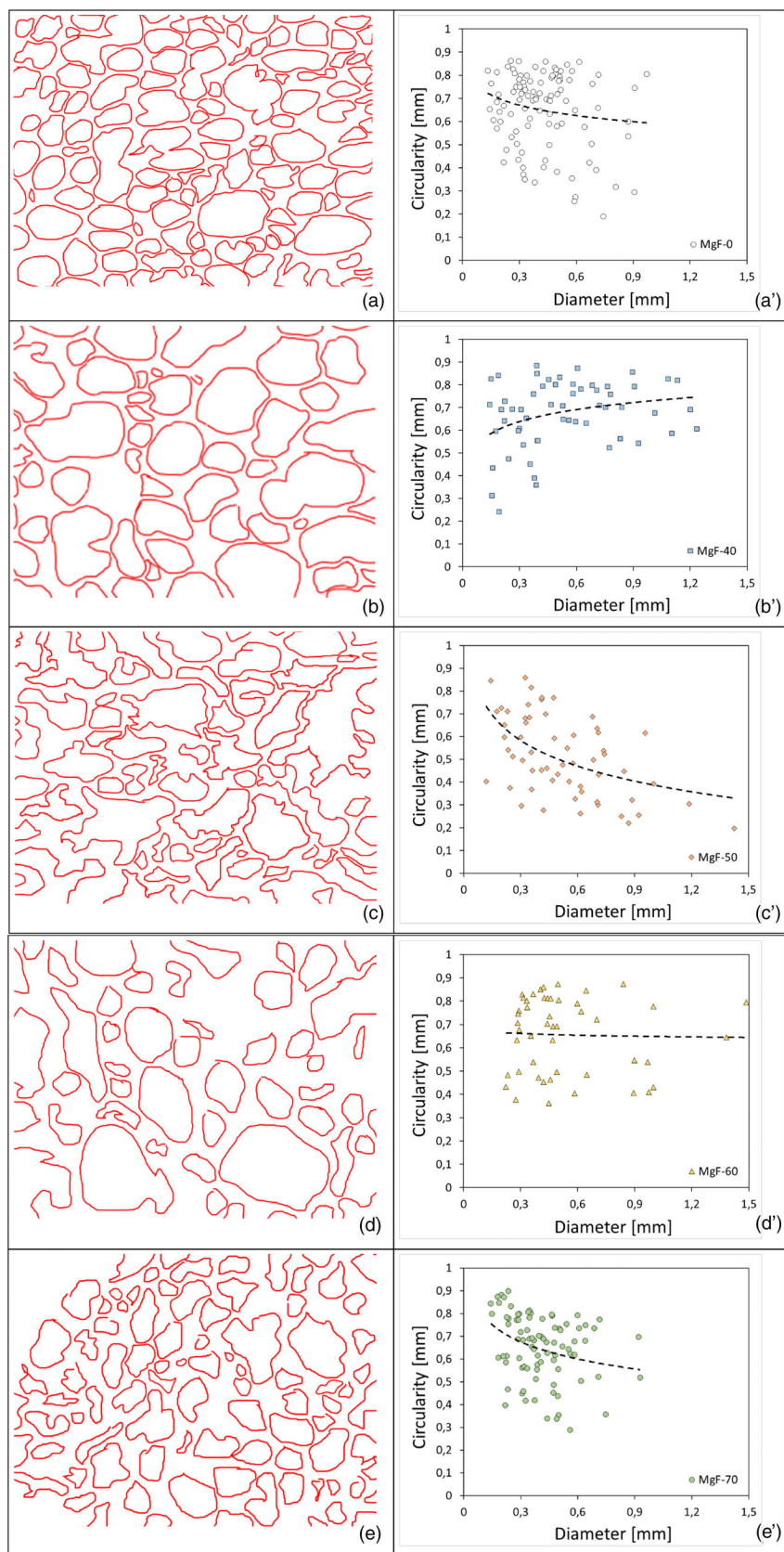


FIGURE 6 Boundary bubble distribution (left) and circularity evolution (right) at varying diameter for all composite foams filled with different salt hydrate content (reference area about 25 mm²): (a,a') MgF-0; (b,b') MgF-40; (c,c') MgF-50; (d,d') MgF-60; (e,e') MgF-70 [Color figure can be viewed at wileyonlinelibrary.com]

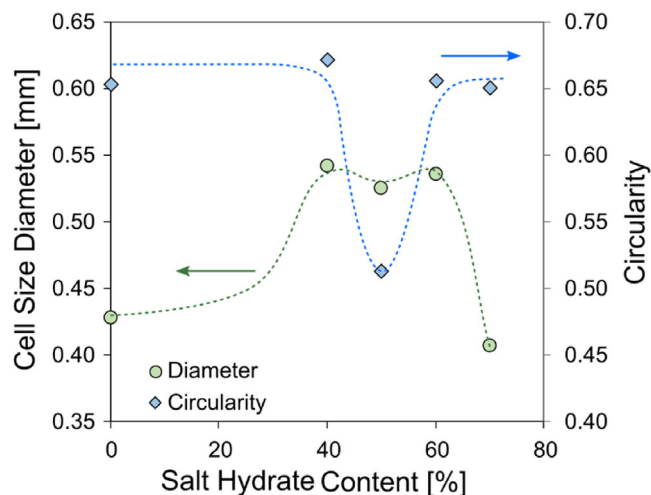


FIGURE 7 Average cell size diameter and circularity at increasing salt hydrate content [Color figure can be viewed at wileyonlinelibrary.com]

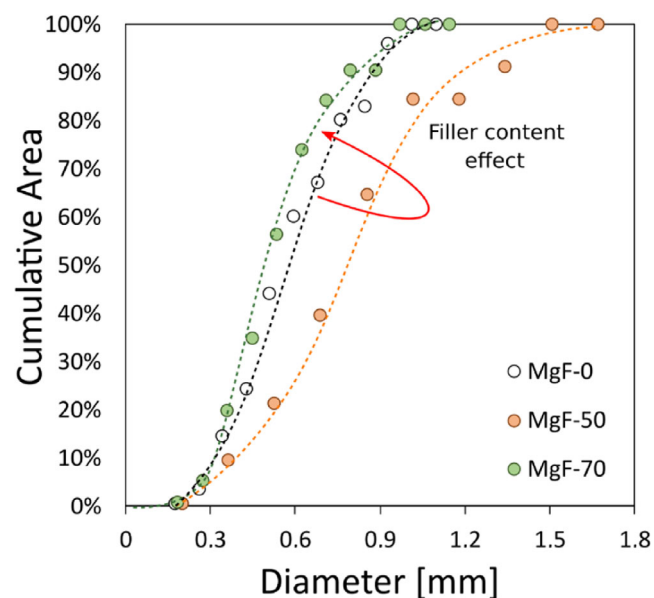


FIGURE 8 Specific cumulative area evolution at varying diameter for three reference foams [Color figure can be viewed at wileyonlinelibrary.com]

the closed mold walls. The result is an incomplete foaming that significantly affects the morphology reducing the average particle.

Concerning the bubble circularity, a clear minimum of this parameter at intermediate filler content (MgF-50) takes place. This behavior can be related to a not complete coalescence process. When the PDMS matrix completed the condensation process, some interconnected bubbles, characterized by a complex and tortuous profile (and low circularity) were stuck in the cross-linked matrix.

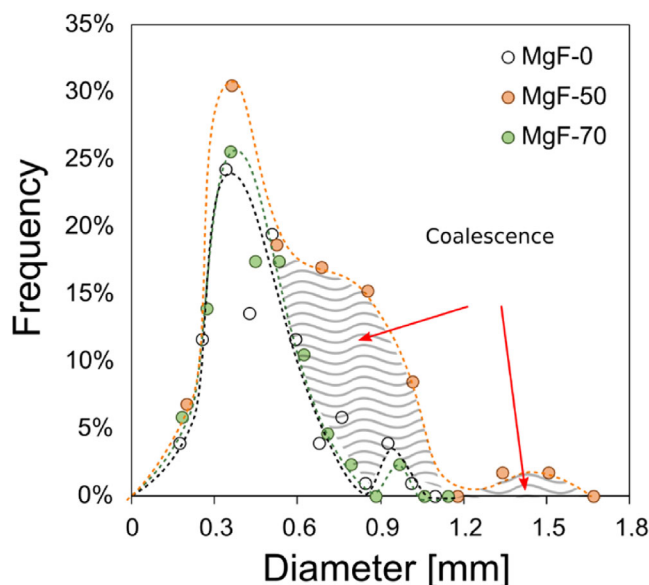


FIGURE 9 Frequency plot of diameter distribution for three reference foams [Color figure can be viewed at wileyonlinelibrary.com]

Instead, in high filled composite foams, due to the high viscosity of the formulation, the coalescence phenomenon is hindered and a large amount of bubbles are characterized by small and circular shape. Consequently, MgF-50 foam represents a threshold formulation characterized by an interconnected cell morphology between regular closed cell structural morphologies (batches at low and high salt content).

Figure 8 compares the evolution of the specific cumulative area at increasing diameter for MgF-0, MgF-50, and MgF-70 samples. It is evident that increasing the salt content in the composite foam the bubble fraction progressively is related to lower size diameter.

Further consideration can be argued evaluating the frequency spectrum of the diameter distribution (Figure 9). The MgF-50 batch has a cluster of bubbles with large diameter, due to a partial (average diameter about 0.9 mm) and complete (average diameter about 1.5 mm) coalescence. Instead, frequency distribution of the other batches is characterized by a single narrow peak at about 0.4–0.5 mm diameter, due to the hampered coalescence phenomenon during the foaming stage.

3.3 | Permeability

Permeability tests were carried out at different flow rates in order to identify the air flow regimes. Existing flow regimes include Darcy, Forchheimer or weak inertial and turbulent flow, depending on the air velocity and thus flow rate.³⁷ For low flow rate conditions, a linear dependence

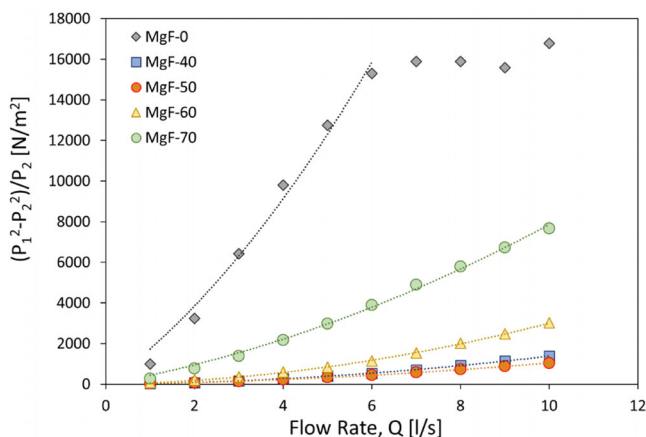


FIGURE 10 Influence of the flow rate on the reduced pressure drop [Color figure can be viewed at wileyonlinelibrary.com]

between the pressure drop and the flow rate is observed according to Darcy equation, which can be expressed as follows for permeability to ideal gases:

$$\frac{P_1^2 - P_2^2}{P_2} = \frac{2 \cdot L \cdot \mu_a}{S \cdot K_D} \times Q \quad (3)$$

where K_D is known as the Darcian permeability, L is the sample thickness, μ_a is the air viscosity, S is the air inlet section, Q is the air flow rate, P_2 is established as atmospheric pressure and P_1 is defined as $P_1 = P_2 + \Delta P$, where ΔP is the pressure drop.

In the Darcy regime, the permeability obtained is most closely related to the internal morphology of the porous medium, and it is likely to be constant for the same porous medium subjected to Darcy flow.

As the flow rate increases, boundary layers begin to develop near solid boundaries inside the porous medium and they become pronounced, and an inertial core appears. The additional drags are captured by another term that has a second-order dependence on the flow rate Q , according to the following equation³⁸:

$$\frac{P_1^2 - P_2^2}{P_2} = \frac{2 \cdot L \cdot \mu_a}{S \cdot K_1} \cdot Q + \frac{2 \cdot L \cdot \rho_a}{S^2 \cdot K_2} \cdot Q^2 \quad (4)$$

where K_1 and K_2 are known as the Darcian and non-Darcian permeabilities, respectively and ρ_a is the air density.

In Figure 10, the reduced pressure drop ($\frac{P_1^2 - P_2^2}{P_2}$) is plotted versus the flow rate. It can be observed that the experimental values follow a second-order dependence with the flow rate meaning that non-Darcy flow is achieved under the experimental conditions. The highest-pressure drop is obtained for the unfilled sample (MgF-0) due to

the presence of highly closed porosity, as observed in SEM images. Consequently, compression of the foam is observed for values of flow rate higher than 6 L/s rather than free air flow through the sample. Regarding the filled foams, a threshold value for linear to non-Darcy regime transition is only observed for the lower salt concentrations being always the threshold flow rate lower than 4 L/s. The transition to inertial and turbulent flow in porous media is characterized by non-uniformity of pore size distribution, internal surface roughness, mixing of intersecting streams, and separation of microscopic flow field from the internal local geometry. From the results, it can be concluded that the morphology modification due to the presence of the salt promotes the non-Darcy flow regime.

The Darcian and non-Darcian permeabilities (K_1 and K_2) were obtained for the fitting curves as follows:

$$\frac{P_1^2 - P_2^2}{P_2} = A \cdot Q + B \cdot Q^2 \quad (5)$$

$$K_1 = \frac{2 \cdot L \cdot \mu_a}{A \cdot S} \quad (6)$$

$$K_2 = \frac{2 \cdot L \cdot \rho_a}{B \cdot S^2} \quad (7)$$

In Table 3, the values for the fitting parameters (A and B , all variables in International System) as well the permeabilities (K_1 and K_2) are shown. All other parameters preserve the same meaning as indicated in Equations (3) and (4). The permeability of porous media mainly depends on the open porosity but also on the tortuosity and roughness of channels interconnecting the pores. The unfilled foam presents the lowest permeabilities due to the closed porosity as mentioned before. The addition of the salt hydrate generates a more porous structure because of the increase of the bubble size distribution in the foaming process. However, as the salt content increases, the porous structure becomes more heterogeneous and the permeability decreases. The results are in agreement, especially for non-Darcian K_2 permeability parameter, with the influence of the salt content on the average cell size in Figure 7 and also with the clogging of pores by the salt particles observed in SEM images (Figure 5).

These considerations can be furthermore assessed evaluating Figure 11 where a correlation between microscopic and macroscopic properties of the composite foams was better addressed. The magnitude of permeability parameters (that can be considered as macroscopic property of the foam) can be related to the intrinsic microstructural porosity of the foam. As reported in other

Sample	A (kg/[s m ⁴])	B (kg/m ⁷)	R ²	K ₁ (m ²)	K ₂ (m)
MgF-0	9.38 × 10 ⁷	6.46 × 10 ¹¹	0.9876	1.58 × 10 ⁻¹¹	3.09 × 10 ⁻⁷
MgF-40	1.21 × 10 ⁶	4.25 × 10 ¹⁰	0.9999	1.24 × 10 ⁻⁹	4.65 × 10 ⁻⁶
MgF-50	1.54 × 10 ⁶	2.87 × 10 ¹⁰	0.9996	9.71 × 10 ⁻¹⁰	6.88 × 10 ⁻⁶
MgF-60	2.44 × 10 ⁶	9.35 × 10 ¹⁰	0.9997	6.09 × 10 ⁻¹⁰	2.13 × 10 ⁻⁶
MgF-70	2.40 × 10 ⁷	1.39 × 10 ¹¹	0.9966	6.19 × 10 ⁻¹¹	1.43 × 10 ⁻⁶

TABLE 3 Fitting parameters and Darcian and non-Darcian permeabilities (K₁ and K₂)

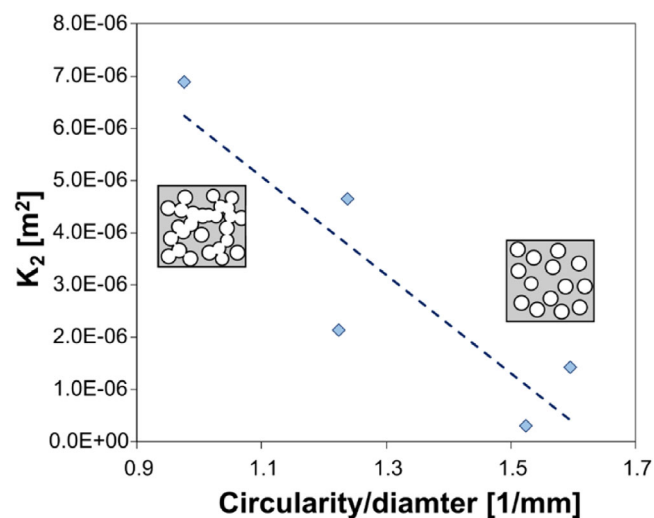


FIGURE 11 Influence of the foam morphology (circularity/diameter ratio) in the non-Darcian permeability (K₂) [Color figure can be viewed at wileyonlinelibrary.com]

foamed structures,³⁹ it should be observed a clear dependence of K₂ with a geometrical parameter of the foam bubble shape (identified as circularity to diameter ratio – x-axis in Figure 11). The effect of the bubble porosity can be justified, at micro-scale level, by considering the variation in the foam wall thickness and the bubble interconnected channels depending on the porosity shape and morphology. Batches with closed and circular shaped morphology evidenced a quite low permeability index. Instead, a progressive increase of K₂ parameter takes place in composite foam characterized by an interconnected morphology, showing a maximum permeability value (6.88 × 10⁻⁶ m) for MgF-50 batch characterized by circularity/diameter parameter equal to 0.98 1/mm, which is over three times higher than the one corresponding to the closed cell structure (state K₂ value).

Based on the promising results achieved, the possibility to identify a correlation between the microstructural parameters of the composite foam with the macroscopic parameters (e.g., foam permeability) is a fundamental precondition, which must be further improved, for the future material design and tailoring according to the specific application requirements. In particular, considering

that in real heat storage applications salt hydrates use water vapor as gaseous sorbate, water vapor permeability measurements are an important point of investigation for the characterization of the material. On this concern, future activities will be focused in order to better address this topic.

In summary, the experimental results obtained on the PDMS-MgSO₄·7H₂O composite foams, state that the choice of hydrated salt content, to encapsulate in the silicone matrix, must be carefully weighted since an excessive amount of filler could not guarantee an adequate encapsulation into the matrix not allowing a suitable foaming process. An intermediate content of hydrated salt, with a threshold value of about 50 wt%, beyond which the composite structure loses its effectiveness in terms of permeability, represents a suitable solution in terms of performance and storage capacity.

Concerning TES applications, an important aspect is the ability to customize the material for each specific application (e.g., charge/discharge capacity) simply by changing the amount of salt inside the composite. Considering that the foamed matrix not hinder the de/hydration capacity of the salt hydrate,²³ storage energy storage density of the chosen optimal composites should be quite in line with those of the pure material. In particular, for this batch a storage energy density equal to 650 kJ/kg (about 300 GJ/m³) is attended (density foam: 0.45 g/cm³ and energy density salt hydrate heptahydrate equal to 2.2 GJ/m³⁴⁰). These values, although slight lower than pure salt, could represent a good industrial compromise in order to preserve a suitable energy storage density and to minimize the undesirable issues of agglomeration, coalescence and corrosion that usually limit the applicability of this salt hydrate.

4 | CONCLUSIONS

A macroporous foamed silicone-based container for MgSO₄·7H₂O salt hydrate was developed for sorption thermal energy storage. In particular, in this article, the relationship between morphological and permeability features of the composite foam at varying filler content (40–70 wt% MgSO₄·7H₂O content) was studied in order to address its applicability of energy storage field.

The morphological analysis showed that all samples exhibited a mixed open/closed porous structure. Preliminarily, the addition of low amount of $\text{MgSO}_4 \cdot 7\text{H}_2\text{O}$ (MgF-40) leads an increase in the bubble size. Afterwards, at increasing salt hydrate amount, a progressive decrease in open porous morphology and pore size was observed. Furthermore, it has been shown that the permeability of porous composite structures depends significantly both on the open porosity and on the tortuosity and interconnection of the foam cavities. The presence of the salt hydrates leads to an increase in permeability, compared to the unfilled one (MgF-0), implying a beneficial action to the water vapor diffusion. The optimal results were found for the MgF-50 foam batch for which a maximum in the non-Darcian permeability was observed. In particular, a K_2 equal to 6.88×10^{-6} m was observed. Based on these results, the circularity/diameter ratio was identified as a bubble shape parameter suitable to discriminate both close to open tortuous microstructure and permeable morphologies.

A threshold salt hydrate content equal to 50 wt% was identified, beyond which the composite structure loses its effectiveness in terms of permeability. For this threshold formulation, a storage energy density equal to 650 kJ/kg (about 300 GJ/m³) is estimated.

These value, could identify a suitable industrial compromise between performance and prevention of undesired issues (such as agglomeration, coalescence, and corrosion) that limit the wide applicability of this salt hydrate.

ACKNOWLEDGMENTS

This work was partially funded by the Ministerio de Ciencia, Innovación y Universidades de España (MCIU/AEI/FEDER, UE) (RTI2018-093849-B-C31) and by the Ministerio de Ciencia, Innovación y Universidades - Agencia Estatal de Investigación (AEI) (RED2018-102431-T). Dr. Luisa F. Cabeza would like to thank the Catalan Government for the quality accreditation given to her research group (2017 SGR 1537). GREiA is certified agent TECNIO in the category of technology developers from the Government of Catalonia. This work is partially supported by ICREA under the ICREA Academia program. Furthermore, special thanks to Dr. Angela Capri who made the composite foam samples used for this experimental campaign. Open Access Funding provided by Università degli Studi di Messina within the CRUI-CARE Agreement.

DATA AVAILABILITY STATEMENT

No. Research data are not shared.

ORCID

Luigi Calabrese  <https://orcid.org/0000-0002-2923-7664>

REFERENCES

- [1] L. F. Cabeza Ed., *Advances in Thermal Energy Storage Systems*, Elsevier, Cambridge, UK **2021**.
- [2] S. Vasta, V. Brancato, D. La Rosa, V. Palomba, G. I. Restuccia, A. Sapienza, A. Frazzica, *Nanomaterials* **2018**, *8*, 522.
- [3] C. W. Chan, J. Ling-Chin, A. P. Roskilly, *Appl. Therm. Eng.*, Vol. 50, **2013**, p. 1257. <https://doi.org/10.1016/j.applthermaleng.2012.06.041>.
- [4] A. Solé, I. Martorell, L. F. Cabeza, *Renew. Sustain. Energy Rev.* **2015**, *47*, 386.
- [5] N. Xie, Z. Huang, Z. Luo, X. Gao, Y. Fang, Z. Zhang, *Appl. Sci.* **2017**, *7*, 1317.
- [6] A.-J. de Jong, H. Fischer, A.-J. De Jong, H. Fischer, *Appl. Sci.* **2018**, *8*, 638.
- [7] P. A. J. Donkers, L. Pel, O. C. G. Adan, *J. Energy Storage* **2016**, *5*, 25.
- [8] H. U. Rammelberg, T. Osterland, B. Priehs, O. Opel, W. K. L. Ruck, *Sol. Energy* **2016**, *136*, 571.
- [9] D. Mahon, G. Claudio, P. C. Eames, *Energy. Conver. Manage.* **2017**, *150*, 870.
- [10] S. K. Henninger, S. J. Ernst, L. Gordeeva, P. Bendix, D. Fröhlich, A. D. Grekova, L. Bonaccorsi, Y. Aristov, J. Jaenchen, *Renew. Energy* **2017**, *110*, 59.
- [11] O. Ola, Y. Chen, Y. Zhu, *Sol. Energy Mater. Sol. Cells* **2019**, *191*, 297.
- [12] Q. Miao, Y. Zhang, X. Jia, L. Tan, Y. Ding, *Sol. Energy* **2021**, *220*, 432.
- [13] S. Hongois, F. Kuznik, P. Stevens, J. J. Roux, *Sol. Energy Mater. Sol. Cells* **2011**, *95*, 1831.
- [14] K. Posern, K. Linnow, M. Niermann, C. Kaps, M. Steiger, *Thermochim. Acta* **2015**, *611*, 1.
- [15] C. Xu, Z. Yu, Y. Xie, Y. Ren, F. Ye, X. Ju, *Appl. Therm. Eng.* **2018**, *129*, 250.
- [16] S. Z. Xu, R. Z. Wang, L. W. Wang, J. Zhu, *Energy* **2019**, *167*, 889.
- [17] Q. Wang, Y. Xie, B. Ding, G. Yu, F. Ye, C. Xu, *Sol. Energy Mater. Sol. Cells* **2019**, *200*, 47.
- [18] W. Li, J. J. Klemeš, Q. Wang, M. Zeng, *Renew. Energy* **2020**, *157*, 920.
- [19] H. A. Ousaleh, S. Said, A. Zaki, A. Faik, A. El Bouari, *Mater. Today: Proc.*, Vol. 30, **2020**, p. 937. <https://doi.org/10.1016/j.matpr.2020.04.354>.
- [20] R. J. Clark, A. Mehrabadi, M. Farid, *J. Energy Storage* **2020**, *27*, 145.
- [21] A. Mehrabadi, M. Farid, *Energy* **2018**, *164*, 194.
- [22] K. Korhammer, M.-M. Druske, A. Fopah-Lele, H. U. Rammelberg, N. Wegscheider, O. Opel, T. Osterland, W. Ruck, *Appl. Energy* **2016**, *162*, 1462.
- [23] Y. Wu, C. Wang, J. Li, Y. Li, *Ind. Eng. Chem. Res.* **2021**, *60*, 1259.
- [24] T. Yan, C. Y. Wang, D. Li, *Appl. Therm. Eng.* **2019**, *150*, 512.
- [25] B. G. P. van Ravensteijn, P. A. J. Donkers, R. C. Ruliaman, J. Eversdijk, H. R. Fischer, H. P. Huinink, O. C. G. Adan, *ACS Appl. Polym. Mater.* **2021**, *3*, 1712.
- [26] H. Wang, Y. Chen, J. Li, L. Guo, M. Fang, *Kona Powder Part J.* **2020**, *37*, 85.
- [27] Lin, S. W.; Lamas, S. V. Air dehydration by permeation through dimethylpolysiloxane/polysulfone membrane article; **2011**; Vol. 55.

- [28] L. Calabrese, L. Bonaccorsi, P. Bruzzaniti, A. Freni, E. Proverbio, *J. Appl. Polym. Sci.* **2018**, *135*, 683.
- [29] V. Brancato, L. Calabrese, V. Palomba, A. Frazzica, M. Fullana-Puig, A. Solé, L. F. Cabeza, *Sol. Energy* **2018**, *173*, 1278.
- [30] L. Calabrese, V. Brancato, V. Palomba, A. Frazzica, L. F. Cabeza, *Sustain. Mater. Technol.* **2018**, *17*, 73.
- [31] L. Calabrese, V. Brancato, V. Palomba, A. Frazzica, L. F. Cabeza, *Sol. Energy Mater. Sol. Cells* **2019**, *200*, 200.
- [32] L. Calabrese, L. Bonaccorsi, A. Freni, E. Proverbio, *Appl. Therm. Eng.* **2017**, *124*, 1312.
- [33] Y. Zhang, M. Ishida, Y. Kazoe, Y. Sato, N. Miki, *IEEE Trans. Electr. Electron. Eng.* **2009**, *4*, 442.
- [34] L. Calabrese, L. Bonaccorsi, A. Freni, E. Proverbio, *Sustain. Mater. Technol.* **2017**, *12*, 27.
- [35] A. K. S. Chesterton, D. A. P. De Abreu, G. D. Moggridge, P. A. Sadd, D. I. Wilson, *Food Bioprod. Process.* **2013**, *91*, 192.
- [36] H. A. Sturges, *J. Am. Stat. Assoc.* **1926**, *21*, 65.
- [37] Ö. Bağcı, N. Dukhan, M. Özdemir, *Transp. Porous Media* **2014**, *104*, 501.
- [38] N. P. Stochero, E. G. de Moraes, A. C. Moreira, C. P. Fernandes, M. D. M. Innocentini, A. P. Novaes de Oliveira, *J. Eur. Ceram. Soc.* **2020**, *40*, 4224.
- [39] O. Smorygo, V. Mikutski, A. Marukovich, A. Ilyushchanka, V. Sadykov, A. Smirnova, *Acta Mater.* **2011**, *59*, 2669.
- [40] V. M. van Essen, H. A. Zondag, J. C. Gores, L. P. J. Bleijendaal, M. Bakker, R. Schuitema, W. G. J. van Helden, Z. He, C. C. M. Rindt, *J. Sol. Energy Eng.* **2009**, *131*, 1014.

How to cite this article: L. Calabrese, L. Hernández, R. Mondragón, L. F. Cabeza, *J. Appl. Polym. Sci.* **2021**, e51924. <https://doi.org/10.1002/app.51924>